

---

Oral presentation | Mesh generation/adaptation

## Mesh generation/adaptation-II

Wed. Jul 17, 2024 2:00 PM - 3:30 PM Room C

---

### [8-C-03] Near-body Mesh Adaption for Transitional Flows using OVERFLOW

\*Balaji Shankar Venkatachari<sup>1</sup>, Joseph M Derlaga<sup>2</sup>, Michael V Donello<sup>2</sup>, Meelan M Choudhari<sup>2</sup> (1. Analytical Mechanics Associates, Inc., 2. NASA Langley Research Center)

Keywords: Boundary-layer transition, transition modeling, mesh adaptation

# Near-Body Mesh Adaptation for Transitional Flows using OVERFLOW

B. Venkatachari\*, M. Donello\*\*, J. Derlaga\*\*, and M. Choudhari\*\*

Corresponding author: balaji.s.venkatachari@nasa.gov

\* Analytical Mechanics Associates, Hampton, VA 23666 USA.

\*\* NASA Langley Research Center, Hampton, VA 23681, USA.

**Abstract:** Accurate modeling of boundary-layer transition is an important aspect of developing greener air transport technologies. In that regard, transition models based on auxiliary transport equations offer a robust approach that is easily integrated into the Reynolds-averaged Navier-Stokes (RANS) solvers. Recent workshops under NATO and AIAA have identified the verification of transport-equations-based transition modeling as a critical aspect of reducing the scatter between the predictions of different CFD codes. Follow-on work has highlighted the need for highly dense grids to achieve an asymptotic convergence of transition related flow metrics. The present work examines the role of automatic near-body mesh adaptation capability in the NASA OVERFLOW CFD solver to enable verification studies in an efficient manner, and for establishing best practices for designing grids for the RANS-based transition models. A sensor function relevant to the Langtry-Menter  $\gamma - Re_{\theta t}$  transition model has been identified and used for error-based mesh adaptation for canonical configurations comprising the flat plate, and the S809 and NLR-7301 airfoils. The efficacy of the mesh adaptation approach is assessed for flow conditions involving multiple transition scenarios such as natural transition, separation-induced transition, and shock-induced transition. The results from this exploratory study indicate that the meshes adapted using the proposed sensor provide solutions that approach the reference solutions obtained with uniformly refined hand-crafted meshes, in terms of the chosen metrics, and yield modest yet significant savings in grid count. We also highlight areas for improvement in the grid adaptation methodology within OVERFLOW.

*Keywords:* Boundary-layer Transition, Transition Modeling, Mesh Adaptation.

## 1 Introduction

Natural laminar flow (NLF) is seen as a significant contributor to the pursuit of sustainable aviation and greener air-transport technologies. One of the main challenges in designing NLF wings is the capability to accurately predict viscous flows with laminar-to-turbulent boundary-layer transition, which has been identified as a critical and pacing item for computational fluid dynamics (CFD) in the NASA CFD Vision 2030 study [1]. Consequently, research on transition models based on the Reynolds-averaged Navier-Stokes (RANS) methodology has been gaining traction. Although this approach does not directly account for the physics of the boundary-layer transition, it is computationally efficient and easy to implement, enabling its adoption in many production CFD solvers.

Some of the commonly used RANS-based transition models include the two-equation  $\gamma - Re_{\theta t}$  model by Langtry and Menter (LM) [2] coupled with the shear-stress transport (SST) RANS model, the Amplification Factor Transport (AFT) model by Coder and Maughmer [3] that was coupled with the Spalart-Allmaras (SA) model, and the SST-coupled one-equation  $\gamma$  model by Menter [4]. The accuracy of these models and the verification of their implementations have been the focus of recent workshops organized by AIAA and NATO AVT-313 workgroups. A major finding from these workshops is the significant scatter amongst results from different codes as the grid was refined. These codes were supposed to have the same nominal implementation of a given transition model, and the same family of grids were used to predict transition over simple canonical geometries. Our recent work [5] examined the primary reasons behind the observed scatter to be (i) an inadequate refinement of grids, and (ii) inconsistencies in implementing the details of the transition model. The outcomes of that work revealed the need for highly dense grids to achieve an asymptotic convergence for a subset of the

relevant metrics. Therefore, the verification of model implementation based on uniform refinement of grids becomes a costly exercise. Furthermore, these findings raise questions about the best practices for designing grids for RANS-based transition models, specifically regarding how reasonably accurate results can be achieved by a practicing engineer in a computationally efficient manner. In this regard, automatic mesh adaptation may be a beneficial strategy to pursue.

Mesh adaptation involves (i) recognizing areas where additional resolution is required, namely feature or error detection; and (ii) a mechanism to alter the mesh, such as r-refinement [6] and h-refinement [7]. Baker [8] provides an extensive review on mesh adaptation approaches as applicable to CFD, while strategies for driving the adaptation process is given in Roy [9]. There are different methods to identify flow regions in need of mesh refinement or coarsening. It can be based on tracking flow quantities/features, solution error estimates, or a goal-based approach using adjoint formulation [10].

Mesh adaptation is seeing an increased use in turbulent flow computations and has been the focus of recent AIAA workshops on high lift prediction [11]. A review on the status of unstructured grid adaptation in meeting the goals of the CFD 2030 vision study can be found in Park et al. [12]. Unlike turbulent flow computations, mesh adaptation for transitional flows has not received much attention, even more so for transitional computations carried out with RANS-based transition models. Recently Hildebrand et al. [13] investigated zonal structured mesh refinement strategies as well as metric-based unstructured grid adaptation for improving convergence of transition-related metrics for the LM model. Gosin et al. [14] explored output-based mesh adaptation on a modified version of the AFT model. Both studies are preliminary in nature but provide valuable insights into the challenges in pursuing mesh adaptation for transitional flows. Given that most of the RANS-based transition models are correlation based, they involve terms that are only  $C^0$ -continuous; this aspect makes it difficult to pursue an adjoint formulation-based adaptation strategy without making substantial changes to the model. On the other hand, while zonal refinement provides significant improvement at a reduced cost, it requires a priori knowledge of the transition zone.

The focus of this work is to examine the automatic near-body mesh adaptation capability of the NASA OVERFLOW [14] CFD solver in the context of the LM transition model, with the goal of efficiently accelerating the grid convergence via improving the mesh resolution in critical parts of the flow field. The near-body mesh adaptation capability [16] in OVERFLOW is built upon the earlier framework developed by Meakin [17] for generating and adapting Cartesian off-body grids. Although adjoint-driven goal-based mesh adaptation is a powerful technique for steady-state flows, computing the adjoint flow solution is a non-trivial task, especially for RANS-based transition models as mentioned earlier. Thus, the mesh adaptation in OVERFLOW relies on simple error estimation based on the local flow solution. The error sensor does not compute the actual error in the solution, but rather relies on the assumption that regions with a large error indicator value may significantly contribute to the overall error in the solution. Thus, these sensors are somewhat heuristic, and the chosen quantity may have limited applicability. In this work, a sensor function relevant to the transition model is identified and used. Isotropic grid refinement (factor of two in each computational coordinate direction) is then applied to regions identified by the sensor, automatically from within the flow solver, by taking advantage of the structured overset grid framework. The present study complements the earlier work by Hildebrand et al. [13], where the more generic Hessian of the Mach number was used for a metric-based anisotropic unstructured mesh adaptation. The assessment of the mesh adaptation approach is carried out based on scenarios involving natural transition, separation-induced transition, and shock-induced transition, using canonical configurations such as a flat plate and well-known airfoils such as the S809 and NLR-7301.

The work is organized as follows. Section 2 provides a short description of the OVERFLOW solver OVERFLOW and the LM transition model. Details on the sensor function and a short description of the adaptation mechanics are presented in Section 3. Section 4 focuses on the results for the flat plate and airfoil configurations. Finally, a summary of the important findings and potential path forward are discussed in Section 5.

## **2 Flow Solver Details**

This section provides a brief description of the NASA CFD solver and the LM transition model.

## 2.1 OVERFLOW

The NASA OVERFLOW code [15] is a finite-difference Navier-Stokes solver that is capable of computing both time-accurate and steady-state solutions on structured overset curvilinear grids via a variety of options for the spatial and temporal discretizations. RANS-based transition models available in OVERFLOW version 2.4c include: (i) the two-equation Langtry-Menter transition model (LM2009) [2] based on the 2003 version of Menter’s SST RANS model [18] along with the modifications proposed by Langtry et al. [19] to account for crossflow induced transition (LM2015), (ii) Coder’s 2017b version of the AFT2017b equation-based model [20] that uses the SA model [21], and (iii) the SA-based Medida-Baeder transition model [22]. Details on the verification of the implemented turbulence models can be found in Ref. [23]. The LM2009 solutions presented here were obtained by running the OVERFLOW 2.4c solver in steady-state mode using low-Mach preconditioning when appropriate, the third-order Roe upwind scheme [24], and the unfactored successive symmetric overrelaxation (SSOR) implicit solution algorithm [25,26]. A third-order discretization was utilized for the convective terms in all the transport equations, while the diffusion terms are evaluated using a second-order accurate discretization. Unless specified, no additional limiters besides those part of the original turbulence/transition model description were used.

## 2.2 SST-based LM model

The original 2009 version of the Langtry-Menter  $\gamma$ - $Re_{\theta t}$  transition model, as described in Ref. [2], includes two transition related transport equations for the intermittency,  $\gamma$ , and the surrogate “transition onset momentum-thickness Reynolds number,”  $\overline{Re_{\theta t}}$ . These two equations are intended to be used in conjunction with the SST-2003 version of the Menter shear-stress transport model [18] that contains two equations for the transport of turbulence kinetic energy (TKE)  $k$  and specific turbulence dissipation rate  $\omega$ . The fundamental correlations in the LM model that determine the transition onset is based upon the local estimates of the streamwise pressure gradient and the turbulence intensity level  $Tu$  (estimated as  $100(2k/(3U^2))^{1/2}$ , with  $U$  being the local velocity). The four transport equations that describe the model are:

$$\frac{\partial(\rho k)}{\partial t} + \frac{\partial(\rho u_j k)}{\partial x_j} = \gamma_{eff} P_{lim} - \min(\max(\gamma_{eff}, 0.1), 1.0) \beta^* \rho \omega k + \frac{\partial}{\partial x_j} \left[ (\mu + \sigma_k \mu_t) \frac{\partial k}{\partial x_j} \right], \quad (1)$$

$$\frac{\partial(\rho \omega)}{\partial t} + \frac{\partial(\rho u_j \omega)}{\partial x_j} = \frac{\alpha}{\nu_t} P_{lim} - \beta \rho \omega^2 + \frac{\partial}{\partial x_j} \left[ (\mu + \sigma_\omega \mu_t) \frac{\partial \omega}{\partial x_j} \right] + 2(1 - F_1) \frac{\rho \sigma_{\omega 2}}{\omega} \frac{\partial k}{\partial x_j} \frac{\partial \omega}{\partial x_j}, \quad (2)$$

$$\frac{\partial(\rho \gamma)}{\partial t} + \frac{\partial(\rho u_j \gamma)}{\partial x_j} = P_\gamma - E_\gamma + \frac{\partial}{\partial x_j} \left[ \left( \mu + \frac{\mu_t}{\sigma_j} \right) \frac{\partial \gamma}{\partial x_j} \right], \quad (3)$$

$$\frac{\partial(\rho \overline{Re_{\theta t}})}{\partial t} + \frac{\partial(\rho u_j \overline{Re_{\theta t}})}{\partial x_j} = P_{\theta t} + \frac{\partial}{\partial x_j} \left[ \sigma_{\theta t} (\mu + \mu_t) \frac{\partial \overline{Re_{\theta t}}}{\partial x_j} \right]. \quad (4)$$

The complete list of the constants, function definitions, boundary conditions, and limiters can be found in Ref. [2] or on the NASA turbulence model resource (TMR)<sup>1</sup> webpage.

## 3 Mesh Adaptation Process

This section provides a short description of the mesh-adaptation process and details on the sensor function used to identify flow regions in need of mesh refinement/coarsening.

### 3.1 Sensor Function

The default sensor function, denoted by  $S$ , in OVERFLOW is the undivided second-difference of the primary flow variables (density, momentum, and stagnation energy per unit volume). As the computed differences are not being divided by the appropriate spatial difference term (say  $\Delta x^2$  for the second difference), we refer to these quantities as “undivided.” Provided the solution is smooth, the undivided difference tends to decay as the grid is refined, unlike a gradient or Laplacian which tends towards its nominal value, indicating a need for further refinement. One example of an early use of the

<sup>1</sup> URL: <https://turbmodels.larc.nasa.gov/> (last accessed June 1, 2024)

undivided difference sensor function can be found in Ref. [27]. However, based on our limited tests with boundary-layer type flows, this sensor function was insensitive to the inner boundary layer, due to linear behavior of the near-wall solution. Provided the initial mesh was under resolved, the adaptation was not triggered until closer to the edge of the boundary layer, leading to inaccurate estimates of the drag coefficient.

The LM and AFT models rely on the vorticity-based Reynolds number as a surrogate for the actual momentum thickness of the boundary layer and to provide the link between the transition onset Reynolds number estimated from an empirical correlation and the local boundary-layer quantities. This quantity reaches a maximum somewhere inside the boundary layer and is the location at which the transition onset is triggered under appropriate conditions. In general, the vorticity is a good quantity to consider for boundary-layer flows. Based on this insight, the sensor function that we found effective for use with these RANS-based transition models is based on the undivided version of the vorticity magnitude, wherein the three vorticity components are computed with central differencing (without being divided by the appropriate spatial differencing term). This baseline function is defined as:

$$S_1 = (\omega_x^2 + \omega_y^2 + \omega_z^2)^{1/2}, \quad (5)$$

where,  $\omega_x, \omega_y,$  and  $\omega_z$  are the three vorticity components (non-dimensionalized) computed using central differencing, e.g.,  $\omega_z = (w_{j+1} - w_{j-1}) / (2\Delta y) - (v_{k+1} - v_{k-1}) / (2\Delta z)$  with the constraint that  $\Delta x = \Delta y = \Delta z = 1$  (and hence it is the undivided difference). Here  $u, v,$  and  $w,$  are the velocity components in the Cartesian coordinates, and the subscripts  $i, j,$  and  $k$  are the grid indices in those directions.

To prevent the sensor being flagged far away from the wall, and to limit the extent of the adaptation,  $S_1$  is augmented with an additional quantity,  $F_{\theta t}$ .  $F_{\theta t}$  is a blending function proposed in the LM model, to keep certain terms only active outside the boundary layer and inactive within it.  $F_{\theta t}$  is defined as:

$$F_{\theta t} = \min \left( \max \left( F_{wake} \cdot e^{-(y/\delta)^4}, 1.0 - \left( \frac{y-1/c_{e2}}{1.0-1/c_{e2}} \right)^2 \right), 1.0 \right) \quad (6)$$

where,  $c_{e2} = 50.0, y$  is the distance to the nearest wall,  $\delta$  is the boundary-layer thickness estimate.  $F_{wake}$  is a function that ensures the blending function is not active in the wake regions downstream of an airfoil and is defined as  $F_{wake} = e^{-((\rho\omega y^2/\mu)/1E+5)^2}$ . Thus, the effective sensor function we use in this work is  $S = S_1 \cdot F_{\theta t}$ . OVERFLOW also has two additional mechanisms (distance weighting and specification of a region) to limit the extent of the adaptation, but they are not used in this work.

### 3.2 Adaptation Process Overview

Once the sensor function (error estimate) has been computed, it is converted into a marker function (after smoothing) that indicates which regions of the grids need be refined or coarsened and by how many levels. This is achieved through use of thresholds set based on the expected drop in error based on the accuracy of the numerical scheme and interpolation procedure utilized. More details on this can be found in Ref. [16]. Then, through use of parametric cubic interpolation, the newer grid system with refined near-body grids is created while trying to honor the smoothness and geometry features of the original grids. Finally, the flow solution is interpolated from the old grid system to the new system.

## 4 Test Cases and Results

All the results in this section are based on steady-state calculations employing the Langtry-Menter transition model coupled with the SST-2003 RANS model. The predicted aerodynamic force coefficients have converged to five significant digits, the L2 norm of the residual for the mean flow equations has been reduced (in an absolute sense) to  $10^{-9}$  or lower, and the residual of the turbulence and transition model equations has been reduced to  $10^{-8}$  or lower. When running test cases with automatic adaptation, the frequency of adaptation was set such that the L2 norm of the residuals for the mean flow and turbulence/transition model equations had also reduced to  $10^{-8}$  or lower. All results were obtained by using the SST turbulence model with sustaining terms [28], to ensure that the turbulence intensity level near the leading edge of the flat plate/airfoil matched the measurement in the experiment. Accordingly, the turbulence intensity  $Tu$  at the inflow/farfield boundary in all the

computations was specified to be the measured value in the experiment and the freestream eddy viscosity ratio  $\mu_t/\mu = 1.0$  based on best practices [29].

As mentioned earlier, OVERFLOW also allows for alternative mechanisms to limit the extent of the adaptation and to use off-body grid adaptation, that may help reduce the overall grid count aggressively. However, those options were not invoked in this explorative phase of the study. Similarly, no attempt was made to gain significant cost advantages over the handcrafted mesh family, by optimizing the time-to-solution when using the adaptation procedure.

#### 4.1 Natural Transition on a Flat Plate

As the first test case, subsonic zero-pressure-gradient boundary-layer flow over a two-dimensional flat plate with a sharp leading edge was computed at flow conditions corresponding to the experimental investigation by Schubauer and Skramstad [30]. The flow conditions studied herein corresponds to  $M_\infty = 0.147$ , unit  $Re = 3.36 \times 10^6/m$ , and  $T_\infty = 288.17$  K. The freestream turbulence intensity,  $Tu$ , in the experiment was 0.1337%.

The computational domain begins 0.15 m upstream of the flat plate leading edge and extends across a plate length of 2.5 m. The top boundary is located 0.3 m from the flat plate. The boundary conditions used are the following: a nozzle inlet condition with a specified total pressure corresponding to the freestream Mach number at the inlet, a Riemann characteristic top boundary, a constant-pressure outflow boundary condition ( $\frac{P}{P_\infty} = 1.0$ ), symmetry on the bottom boundary upstream of the flat-plate leading edge, and a viscous adiabatic wall boundary condition on the plate. Details of the baseline handcrafted grid family are listed in Table 1. The grid size doubled between consecutive even or odd levels and each even level grid was obtained through uniform refinement with a factor of 4/3 from the previous odd level grid. The fifth mesh level in this case had a near-wall spacing of  $4 \times 10^{-6}$  m that corresponded to a  $y^+ \approx 0.25$  (estimated based on the flat-plate boundary-layer theory at the transition onset location). The third level mesh served as the baseline mesh for the sensor-based adaptation study.

Figure 1 shows the evolution of the intermittency variable ( $\gamma$ ), the baseline mesh (level 3) and the regions of refinement identified by the sensor (four levels of refinement in this case). Recall that, in the LM model,  $\gamma = 1$  in the freestream, 0 within the laminar boundary layer, and grows from 0 to 1 somewhere in the middle of the laminar boundary layer upon meeting transition onset conditions. From Fig. 1(b), one can clearly see that the proposed sensor tracks the growth of intermittency within the boundary layer, given how the transition onset is dependent on the vorticity-based Reynolds number. Consequently, the grids get refined within the boundary layer and around the edge of the boundary layer ( $y > 0.005$  in the fully turbulent region with  $x > 1.0$ ). Although not obvious from the figure, there is a significant amount of refinement near the leading edge as well.

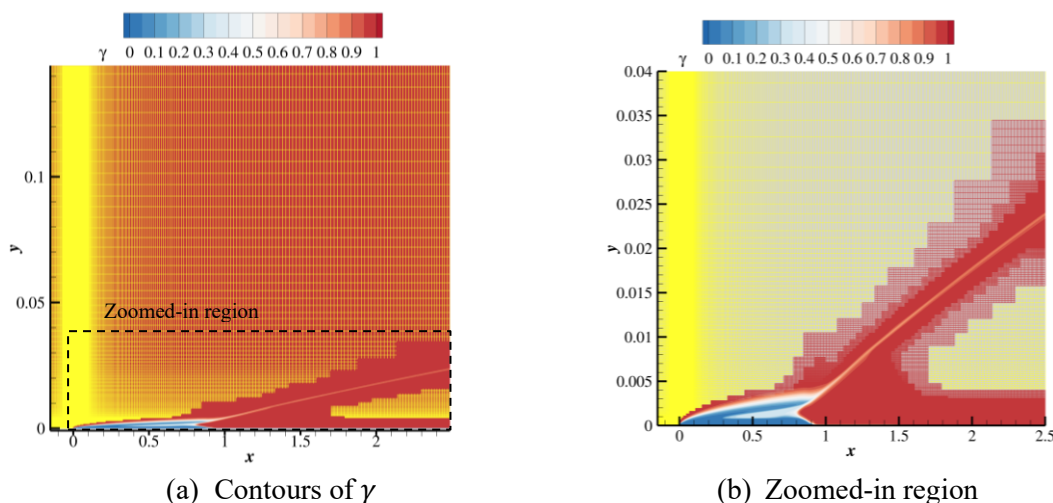


Figure 1. Contours of the intermittency variable  $\gamma$  obtained using the LM model for a flat plate with mesh adaptation. The baseline level 3 mesh is shown as yellow grid lines. The adapted mesh with three levels of refinement is colored with  $\gamma$  in the zoomed-in view.

Table 1. Schubauer and Skramstad flat plate handcrafted mesh dimensions.

Mesh Level	No. of points in the streamwise direction	No. of points in the wall-normal direction	Points upstream of the leading edge
Mesh 1	181	97	49
Mesh 2	241	129	65
Mesh 3	361	193	97
Mesh 4	481	257	129
Mesh 5	721	385	193
Mesh 6	961	513	257
Mesh 7	1441	769	385
Mesh 8	1921	1025	513
Mesh 9	2881	1537	769
Mesh 10	3841	2049	1025

Figure 2 shows the grid convergence of the streamwise evolution of  $C_f$  and the drag coefficient  $C_D$  obtained with the handcrafted mesh family, as well as the adapted meshes. Also shown in Fig. 2(b) is the predicted  $C_D$  that may be obtained with infinite resolution using the Richardson extrapolation procedure. As was previously observed in Ref. [5], the results obtained with the handcrafted mesh family indicated grid convergence, in terms of the streamline evolution of the skin-friction coefficients, at mesh levels above three. However, the drag coefficient continues to change for the solutions obtained with mesh levels above three, with a difference of nearly half a drag count between the results obtained with mesh levels three and ten. The streamwise evolution of skin-friction coefficients obtained with the adapted meshes show good convergence, and only minor differences can be observed. In terms of  $C_D$ , the values increase with additional levels of refinement, approaching the expected value at infinite resolution, for smaller values of  $h$ , as compared to that from the uniformly refined grid. For comparison, the mesh with three levels of refinement had nearly 75% fewer grid points than the level 9 mesh (level 3 mesh + three levels of uniform refinement across the entire domain). Thus, indicating a potential benefit of using mesh adaptation in the verification studies of such RANS-based transition models. As indicated by Hildebrand et al. [13], for this test case, refinement in the wall-normal direction had a significant impact on the asymptotic convergence of the drag coefficient, compared to streamwise refinement. In their study, the grid was manually refined only around the transition zone. However, in the present study, we are unable to discern the importance of resolution in any one particular direction, given that the adaptation process implemented in OVERFLOW is isotropic.

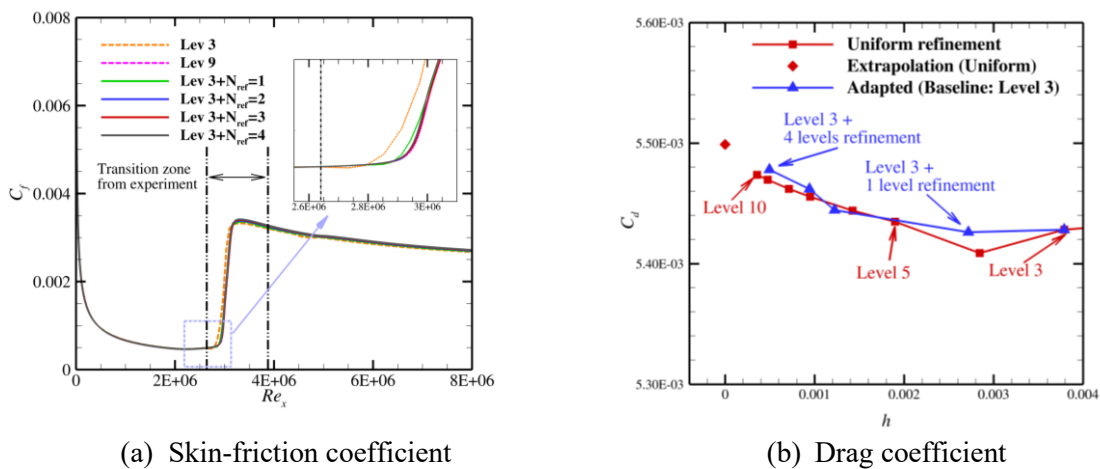


Figure 2. Plots of grid convergence of the skin-friction and drag coefficients for a flat plate, undergoing natural transition, obtained with the LM model using both uniformly refined (handcrafted) and adapted meshes. Grid sizing parameter  $h = 1/\sqrt{N}$ ;  $N$  being the total number of grid points and  $N_{ref}$  = number of levels of refinement.

Model accuracy is not the focus of this study. However, the transition onset predicted by the model (the location of the rise in the skin-friction from its laminar value in Fig. 2(a)) obtained with these adapted meshes falls within the transition zone identified from the experiment, but the predicted width of the transition region is significantly narrower.

## 4.2 Subsonic S809 Airfoil

The S809 airfoil was designed for wind-turbine applications and the data from the experiments involving this airfoil [31] is often used for the validation of transition models. The experiments were carried out in the low-turbulence wind tunnel (freestream turbulence intensity of 0.02%) at Delft University. For most of the conditions tested during the experiment, transition on both the upper and lower surfaces of the airfoil is caused by the appearance of a small laminar separation bubble on each respective side. The flow condition studied here correspond to  $M_\infty = 0.1$ ,  $Re_c = 2.2 \times 10^6$ ,  $\alpha = 1^\circ$ ,  $T_\infty = 300\text{K}$ , and  $Tu_\infty = 0.07\%$ .

The baseline grids were of C-grid topology, details of which are given in Table 2. The grid count in both streamwise and wall-normal directions doubled in size with every level of refinement. Mesh level 4 has a near wall spacing of  $1.15 \times 10^{-6}$  chord length, yielding  $y^+ \sim 0.1$  (at mid-chord location based on fully turbulent flat-plate correlations) for  $Re_c = 2.2 \times 10^6$  and had approximately 200 points within one boundary-layer thickness (based on the mid-chord estimate). The finest grid was generated first, based on established best practices of grid generation for using these transition models, and the rest of the family was obtained by coarsening it systematically. The outer boundary was located at 1000 chord lengths away. These grids were sized based on the grids generated by the AIAA Transition Modeling and Prediction Workshop committee [32]. The two coarsest meshes are intentionally slightly coarser (in the wall-normal direction) than what was used in an earlier study on the NLF-0416 airfoil [5], so as to keep the grid count smaller and similar to what a practicing CFD engineer is likely to use.

The results from the baseline grids were used as reference values, while mesh levels 1 and 2 were used as the initial grids for the mesh adaptation study. The grid convergence of the pressure and skin-friction coefficients obtained with the hand-crafted grids and the finest adapted mesh obtained with level 1 (with 3 levels of refinement) and level 2 (with 2 levels of refinement) are shown in Fig. 3(a) and 3(b). The upper surface experiences a gradual favorable pressure gradient before encountering a sharp adverse pressure gradient around the mid-chord section, while the lower surface undergoes sharper acceleration, before experiencing an adverse pressure gradient region at around 40% chord location, as seen from Fig. 3(a). This pressure profile leads to a laminar separation bubble on both the top and the bottom surface, as indicated by the skin-friction plot in Fig. 3(b). In terms of the convergence of  $C_p$ , from Fig. 3(a) it can be observed that except in the vicinity of where the adverse pressure gradient region starts, results from all the meshes lie on top of one another and closely match the measured data. Results from mesh level 3 and above, along with finest adapted mesh from each mesh family, lie on top of one another, even in the region where the adverse pressure gradient starts and is the location of the transition onset. This is confirmed by the skin-friction distribution plots as well as the zoomed-in insets shown in Fig. 3(b).

Table 2. Dimensions of the handcrafted meshes for the S809 and NLR-7301 airfoils.  $N_x$ : streamwise resolution;  $N_y$ : wall-normal resolution;  $N_{wake}$ : wake resolution.

Mesh Level	S809			NLR-7301	
	$N_x$	$N_y$	$N_{wake}$	$N_x$	$N_y$
Mesh 1	353	49	49	307	169
Mesh 2	705	97	97	613	337
Mesh 3	1409	193	193	1225	673
Mesh 4	2817	385	385	2449	1345

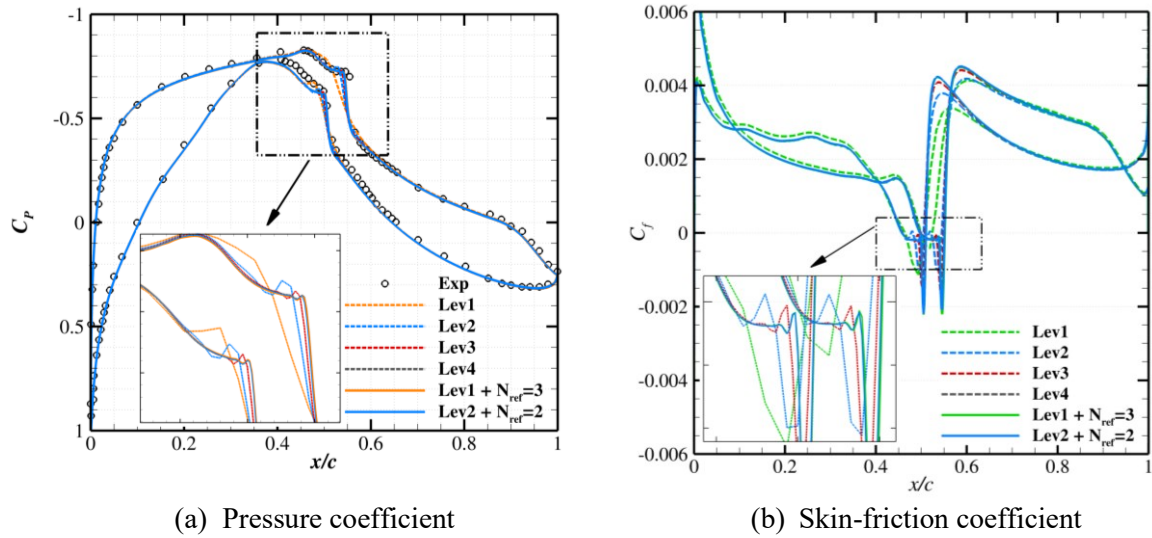


Figure 3. Plots of grid convergence of the pressure and skin-friction coefficients for the S809 airfoil at  $\alpha = 1^\circ$  and  $Re_c = 2.2 \times 10^6$ .

The mesh count and associated reductions for the adapted grids are listed in Table 3. As inferred from Table 2, the adapted mesh obtained with one level of refinement when starting with the level 1 mesh has a grid count that is nearly the same as the level 2 mesh obtained with manual uniform refinement in both directions. Although a level 1 baseline mesh followed by one level of global refinement everywhere, should be identical to the level 2 mesh from the hand-crafted mesh family, we see from Table 3, that we end up with an increased grid count (negative savings). This arises from OVERFLOW needing fringe points, and hence the adaptation regions can expand past the desired refinement regions leading to a marginal increase in the grid count. This indicates that the baseline level 1 mesh is very coarse and not adequate for obtaining a reasonable solution. As can be observed from Table 2 and Fig. 4 (a), mesh level 1, even with three levels of refinement, results in a modest  $\sim 25\%$  savings (as compared against mesh level 4 that is representative of mesh 1 with three levels of uniform global refinement) unlike in the case of the flat plate. Even mesh 2 with two levels of refinement results in only 17% savings.

Table 3. Dimensions of the handcrafted mesh family and the adapted meshes for the S809 airfoil.

Baseline mesh level	Grid Count	Baseline Mesh level 1	Adapted Grid Count	Savings (%)	Baseline Mesh level 2	Adapted Grid Count	Savings (%)
1	17297	$N_{\text{ref}}=0$	17297	0.000			
2	68385	$N_{\text{ref}}=1$	69702	-1.926	$N_{\text{ref}}=0$	68385	0.000
3	271937	$N_{\text{ref}}=2$	237387	12.705	$N_{\text{ref}}=1$	232809	14.389
4	1084545	$N_{\text{ref}}=3$	821514	24.253	$N_{\text{ref}}=2$	898845	17.122

Similar to the flat plate case, the adapted regions are colored by  $\gamma$  in Figs. 4 and 5, while the unrefined regions are colored in solid yellow. It can be seen from Figs 4(a) and 4(b), the refinement region extends up to a distance of approximately fifty chord lengths away from the airfoil. This is counterintuitive as one would expect the grid refinement to be primarily confined to the vicinity of the airfoil, indicated by the green box region in Fig. 4(a). In the case of level 1 baseline mesh undergoing three levels of refinement, we observe that finest refinement region (marked as level 3 refinement region in Fig. 4(a)) extends as far as twenty chord lengths away from the airfoil. The zoomed in plots in Figs. 5(a)–5(c) indicate that much of the highly refined regions are within the boundary layer (indicated by the region where  $\gamma$  grows from 0 (blue) to 1 (red)) and some additional regions near the leading and

trailing edge of the airfoil. However, the coarser wall-normal resolution outside of the boundary layer in the underlying baseline mesh along with the fringe-point requirements of the solver, mentioned earlier, causes the adaptation regions to expand past the desired refinement region.

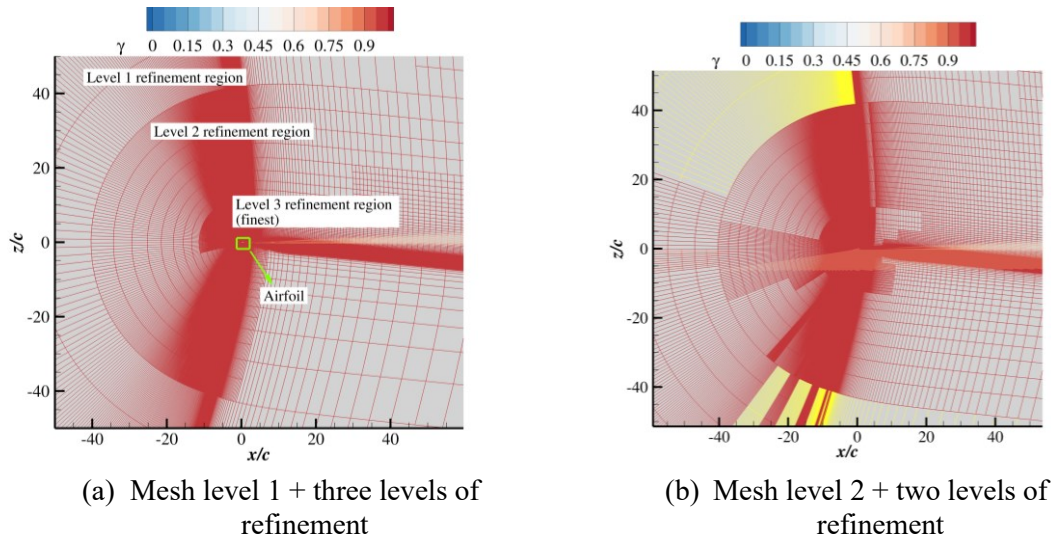


Figure 4. Overview of the adapted meshes for the S809 airfoil. The baseline mesh used for the adaptation (level 1 or 2 mesh) is shown as yellow grid lines. The refined mesh regions are colored with  $\gamma$ .

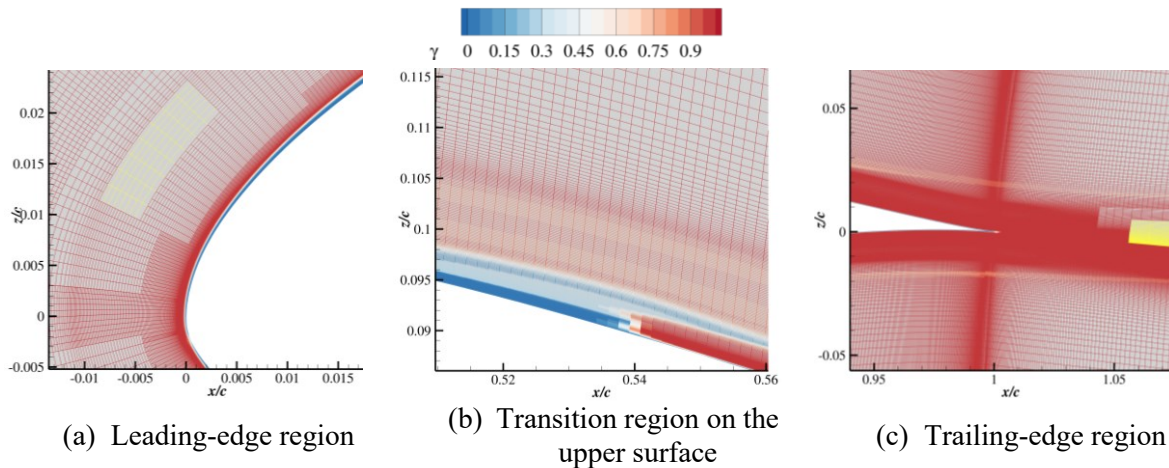


Figure 5. Zoomed-in view of the adapted mesh obtained after two levels of refinement of baseline level 2 mesh. The refined regions are colored with  $\gamma$ . The unrefined region is indicated in yellow.

Plots illustrating the grid convergence of the lift coefficient,  $C_L$ , and the drag coefficient,  $C_D$ , obtained with the handcrafted mesh family and the adapted meshes are shown in Fig. 6. With uniform refinement, the lift and drag coefficients appear to be heading towards convergence with baseline mesh levels 3 and 4; although one may need additional finer meshes to confirm the trend. While the sequence of meshes resulting from adapting the baseline mesh level 1, do converge in terms of the drag coefficient, the lift coefficient obtained after three levels of refinement seems to be diverging and smaller than that obtained with the globally refined meshes. As for the results obtained with meshes adapted based on the level 2 mesh, both lift and drag coefficients are reasonably close to the reference prediction based on the finest uniformly refined grid. Although not shown here, the level 2 mesh with 3 levels of refinement (34 % savings in grid count) also resulted in a lift coefficient that was slightly lower than that obtained using the level 4 mesh, along with a non-monotonic trend. However, the difference between the values was much smaller. A possible reason for not achieving a cleaner convergence trend of the lift coefficient may be related to the cubic interpolation process used in the

adaptation process [16], which could alter the geometry near regions of sharp changes in curvature (such as the leading and trailing edge regions) resulting in changes to the overall circulation, and hence to the lift. At times, this resulted in adaptation cycles that alternated between refinement and coarsening of these mesh regions, preventing the grid count from reaching a clear asymptote. This observation requires additional investigation.

Based on the results concerning the convergence of the force coefficients and the discussion earlier, it can be concluded that for this case, mesh level 3 or finer is required to be able to explore proper verification of the LM model. Although the finer resolution baseline meshes and the meshes resulting from adapting baseline mesh level 2 provide a reasonably grid-insensitive solution for this case with the LM model, it would be useful to explore additional meshes of the hand-crafted mesh family (with finer resolutions) and mesh families derived from applying automatic mesh adaptation, so as to perform a Richardson extrapolation analysis.

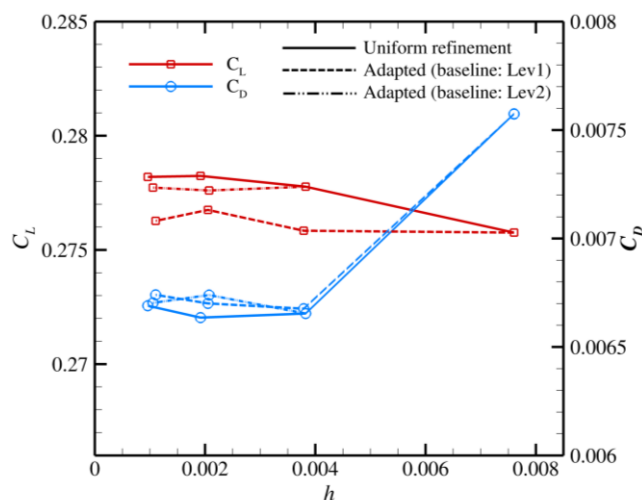


Fig. 6. Plots of grid convergence of the lift and drag coefficients for the S809 airfoil obtained with the LM model using both uniformly refined (handcrafted) and adapted meshes. Grid sizing parameter  $h = 1/\sqrt{N}$ .

### 4.3 Transonic NLR-7301 Airfoil

The third test case examined in the present study is the supercritical airfoil NLR-7301, with a maximum thickness of 16.5% relative to the chord length. Transition measurements are available from the experiments carried out at the National Aerospace Laboratory of Netherlands (NLR) [33] over a range of Mach numbers and angles of attack, albeit at a low Reynolds number of approximately 2.2 million. The combination of large airfoil thickness and the flow conditions chosen for the experiment causes dramatic variations in the transition location, even with small changes in flow parameters near the shock-free design condition. The apparently large sensitivity of the transition location in this test case makes it challenging for the existing transition models.

The flow condition studied here corresponds to  $M_\infty = 0.748$ ,  $Re_c = 2.2 \times 10^6$ ,  $T_\infty = 300K$ ,  $\alpha = -2.267^\circ$ , and  $Tu_\infty = 0.158\%$ . These conditions result in a separation-bubble induced transition on the upper surface and transition due to shock-induced separation on the lower surface of the airfoil. The baseline grids were of O-grid topology, given that the trailing edge is of finite-thickness. Details about the grid resolution are given in Table 2. The grid count in both streamwise and wall-normal directions doubled in size with every level of refinement. Mesh level 4 has a near-wall spacing of  $6.2 \times 10^{-7}$  chord, yielding  $y^+ \sim 0.0625$  (at mid-chord location based on fully turbulent flat-plate correlations) for  $Re_c = 2.2 \times 10^6$ . It also contained 49 points in the trailing edge and nearly 600 points within the boundary layer (based on the mid-chord estimate). The outer boundary was located 1000 chord lengths away. Here again, mesh level 4 (the finest grid) was generated first, and the rest of grid

the family was obtained by coarsening it systematically. These meshes have higher wall-normal resolution than the S809 case.

Mach number contours are shown in Fig. 7 and reveal the presence of a shock along the lower surface. The upper surface experiences a mild favorable pressure gradient downstream of the suction peak, before encountering an adverse pressure gradient region at around the 70% chord location, leading to a separation-bubble induced transition as seen from the pressure and skin-friction coefficient distributions shown in Fig. 8(a) and (b). From Fig. 8(a), the lower surface also experiences a mildly favorable pressure gradient region downstream of the leading edge before encountering a shock around the mid-chord region. The shock causes the boundary layer to separate ahead of the shock and quickly undergoes transition, as seen from Fig. 8(b).

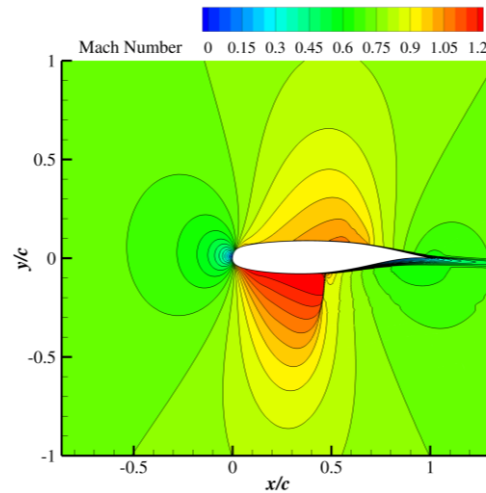


Fig. 7. Mach number distribution around the NLR-7301 airfoil for  $M_\infty = 0.748$ ,  $Re_c = 2.2 \times 10^6$ , and  $\alpha = -2.267^\circ$ .

The results from the baseline grids were used as reference values, while mesh levels 1 and 2 were used for the mesh adaptation study. The grid convergence of the pressure and skin-friction coefficients obtained with the hand-crafted grids and the finest adapted mesh obtained starting with mesh level 1 (with 3 levels of refinement) and level 2 (with 2 levels of refinement) are shown in Fig. 8(a) and 8(b). The experimentally measured  $C_p$  is also included in Fig. 8(a) for reference. In terms of the convergence of  $C_p$ , from Fig. 8(a) it can be observed that, except in the vicinity of where the adverse pressure gradient region/shock starts (see the zoomed-in inset in Fig. 8(a)), results from all the meshes lie on top of one another and closely match the measured data. Except in the region around the shock on the lower surface, the  $C_p$  distribution predicted by the LM model on these meshes also closely matches the data from the experiment. In general, the LM results obtained with mesh level 2 and finer resolution meshes, along with the finest adapted mesh from each mesh family, lie on top of one another even in the start of the adverse pressure region- the location of transition onset. This is also confirmed by the skin-friction distribution plots as well as the zoomed-in insets shown in Fig. 8(b). Minor differences do exist in the evolution of the skin-friction coefficient within the bubble.

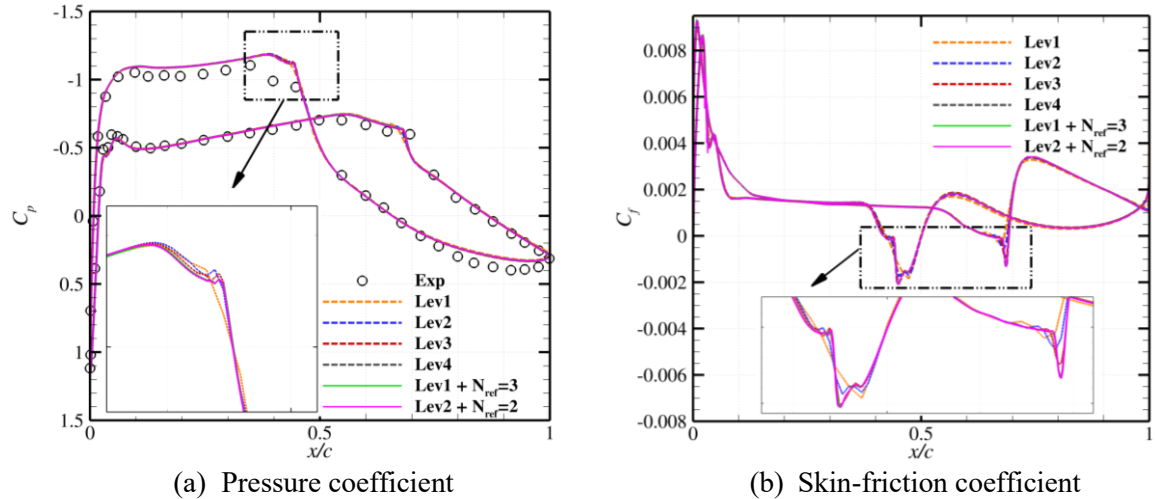


Figure 8. Plots of grid convergence of the pressure and skin-friction coefficients for the NLR-7301 airfoil at  $\alpha = -2.267^\circ$ ,  $M_\infty = 0.748$ , and  $Re_c = 2.2 \times 10^6$ .

The mesh count and savings obtained with the adaptation process are listed under Table 4. Unlike the case of the S809 airfoil, we start getting savings of 15% even with one level of refinement on the level 1 mesh, and up to 35% with additional refinement. A likely reason for this could be related to the apparently increased wall-normal resolution of the baseline meshes in the present case. Fig. 9 shows the overview of two adapted meshes and a zoomed-in view of the region around the airfoil. As mentioned previously, the increased wall-normal resolution of the level 1 baseline mesh (compared to the S809 airfoil) results in more confined regions of adaptive grid refinement. Even with three levels of refinement, the bulk of the refinement region only extends as far as 5 chord lengths away from the airfoil, as seen from the unrefined yellow region in Fig. 9(a). Using mesh level 3 for the adaptation, the region of adaptation shrinks even more, restricted to being just around the boundary-layer region (region where  $\gamma$  grows from 0 (blue) to 1 (red)) on the upper surface, and upstream of the shock on the lower surface. The shock along the lower surface generates additional vorticity and also influences the production and transport of intermittency. As the sensor used for the adaptation is dependent on these quantities, refinement is triggered over a larger wall-normal direction in the post-shock region on the lower surface (as can be seen from the zoomed-in region of Fig. 9). In general, it can be concluded that the sensor is working well for this case, in terms of savings in grid count.

Table 4. Dimensions of the handcrafted and adapted meshes for the NLR-7301 airfoil.

Baseline mesh level	Grid Count	Baseline Mesh level 1	Adapted Grid Count	Savings (%)	Baseline Mesh level 2	Adapted Grid Count	Savings (%)
1	51883	$N_{\text{ref}}=0$	51883	0.000	$N_{\text{ref}}=0$	206581	0.000
2	206581	$N_{\text{ref}}=1$	175398	15.09	$N_{\text{ref}}=1$	602721	26.89
3	824425	$N_{\text{ref}}=2$	593845	27.97	$N_{\text{ref}}=2$	2056801	37.56
4	3293905	$N_{\text{ref}}=3$	2127232	35.42			

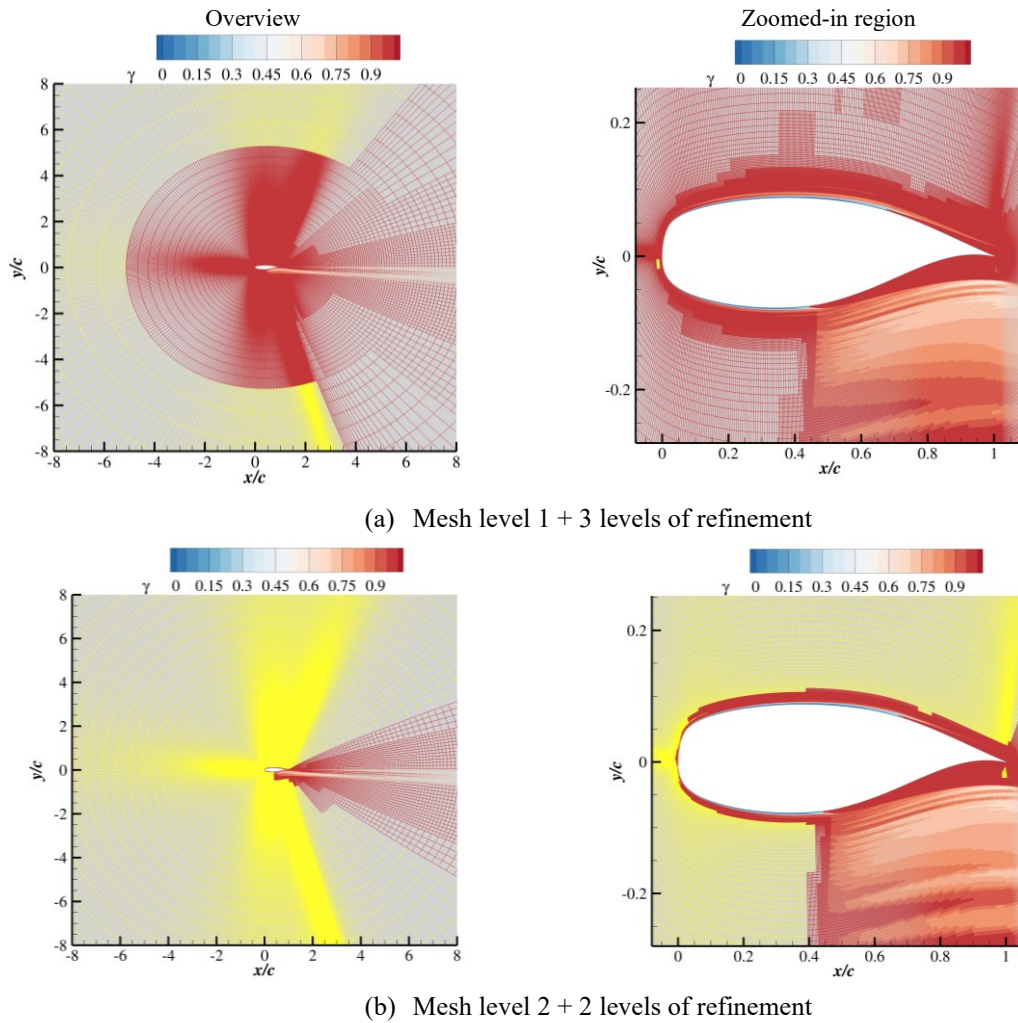


Figure 9. Snapshots of the adapted meshes for the NLR-7301 airfoil. The baseline mesh used for the adaptation (level 1 or 2 mesh) is shown as yellow grid lines. The refined mesh regions are colored with  $\gamma$ .

Plots showing the grid convergence of the lift and drag coefficients obtained with the handcrafted meshes and the adapted meshes are shown in Fig. 11. It may be observed that the drag coefficients obtained with globally refined meshes become relatively grid-insensitive to the resolution level when the baseline mesh level equals 3 or higher. For the automatically adapted meshes, when starting from the baseline mesh level 1, two levels of refinement are required to reach this behavior while one level of additional refinement is needed when starting with mesh level 2, to achieve  $C_D$  values that are closer to the predictions based on levels 3 and 4 of the handcrafted mesh family. However, the difference between  $C_D$  obtained with automatic adaption of baseline level 1 mesh and the reference value obtained with an equivalent uniformly refined mesh is larger than that obtained via automatic adaptation from the baseline level 2 mesh. The  $C_L$  predictions from the hand-crafted mesh family indicate an oscillatory behavior, although the differences between the results obtained with different meshes are not too far apart. The  $C_L$  predictions obtained with automated adaptation starting from baseline mesh level 2 are closer to those from levels 3 and 4 of the handcrafted mesh families. In general, adapted meshes using the level 2 mesh as baseline give a much closer match in force coefficients to those obtained with the uniformly refined meshes. However, again, additional refinement (followed by Richardson extrapolation analysis) is necessary to confirm this trend and check for the asymptotic convergence.

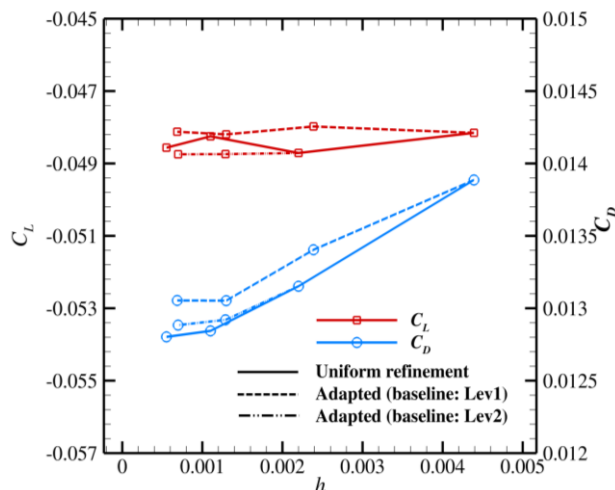


Fig. 10. Plots of grid convergence of the lift and drag coefficients for the NLR-7301 airfoil obtained with the LM model using both uniformly refined (handcrafted) and adapted meshes. Grid sizing parameter  $h = 1/\sqrt{N}$ .

## 5 Summary and Conclusions

In this work, the automatic near-body mesh adaptation capability of NASA's OVERFLOW CFD solver was explored for the Langtry-Menter transition model, with the goal of accelerating the grid convergence of RANS-based transition models by fine-tuning the meshes in critical parts of the solution. Using error indicators, the adaptation process in OVERFLOW performs isotropic grid refinement, i.e., by a factor of two along each computational coordinate. Given that the vorticity-based Reynolds number serves as a critical quantity in the LM transition model (as well as in other local-correlation-based transition models), an error sensor based on the undivided difference of the vorticity magnitude was evaluated as part of this work, using benchmark 2D test cases such as the flat plate, a subsonic airfoil (S809) and a transonic airfoil (NLR-7301). For all test cases studied here, handcrafted meshes with different levels of uniform refinement in both directions were utilized as the baseline grids for further automated refinement and the solutions of those handcrafted grids were employed as the basis for assessing the efficacy of automated grid refinement. The metrics for assessment included the global force coefficients, along with streamwise distributions of pressure and skin-friction coefficients, and how the results from the automatic adaptation approached those from equivalent handcrafted grids.

For the flat plate undergoing natural transition, the vorticity-magnitude-based sensor function led to mesh refinement within the boundary-layer region, which is obviously important for a transition model, as well as in the leading-edge region. In this case, grid converged predictions of transition onset location and drag coefficient were obtained with 75% fewer grid points than handcrafted meshes with uniform refinement everywhere.

The second test case of subsonic flow over a S809 airfoil involved separation-induced transition on both surfaces of the airfoil. A family of baseline meshes with a C-grid topology and four levels of uniform refinement was used. The coarsest baseline mesh had slightly coarser wall-normal resolution than what has been recommended for use with these transition models in previous studies. When the adaptation is carried out using the coarsest of the baseline meshes, the adaptation process refined the mesh almost everywhere (including the free stream region). Even though the sensor correctly flags the boundary-layer region in need for refinement, because of the lack of resolution outside the boundary layer, and the interpolation requirements of the overset procedure (overlap needed between consecutive mesh refinement levels), additional refinement regions are added far outside the boundary layer. Therefore, unlike the flat-plate case, no appreciable savings in grid count were gained for this test case. Furthermore, when three or more refinement levels are sought using a very coarse baseline mesh, the parametric cubic interpolation procedure used to create the refined near-body grids led to meshes being alternatively refined and coarsened with each adaptation cycle. This occurred specifically near regions of sharp changes in curvature, and as a result, the grid count did not asymptote. This aspect in turn led

to an oscillatory convergence of the lift coefficient and needs further investigation. The second coarsest mesh was identified as the minimum resolution needed to obtain a reasonably accurate solution and for the force coefficients to approach the reference values obtained with finer meshes from the family of globally refined meshes.

The supercritical NLR-7301 airfoil under transonic conditions served as the final test case. At the negative angle of attack for this case ( $\alpha = -2.267^\circ$ ), the upper surface shows shock-free pressure recovery, but the flow over the lower surface develops a shock and the boundary layer transitions due to shock-induced separation. Given the moderate Reynolds number ( $Re_c = 2.2 \times 10^6$ ) of the flow, the upper surface boundary layer remains laminar until the suction peak and transitions due to flow separation near the beginning of the pressure recovery. Here, four baseline meshes of O-grid topology, with each mesh being uniformly refined in both coordinate directions from the previous level, was used. These meshes had significantly more points in the wall-normal direction than the S809 case, while the streamwise resolution was similar. Thus, even when the coarsest mesh was used as the starting point for the adaptation process, the refinement region identified by the chosen sensor was limited just 5 chord lengths away from the airfoil. When the second coarsest mesh was used, bulk of the flagged regions were restricted to the boundary-layer region and the regions around the leading and trailing edges. A 35% reduction in grid count was achieved for this test case. When the automatic adaptation process was started from the second coarsest mesh, the pressure, skin-friction and force coefficients were closer to the results from uniform refinement.

Overall, the proposed vorticity-based sensor, was able to both identify critical regions of the flow and adapt the mesh to accelerate the progress of the LM solutions towards resolution-insensitive flow behavior at a reduced cost. For both airfoil test cases, the finest levels of globally refined meshes were not sufficient to demonstrate asymptotic convergence of the predicted force coefficients. Additional refinement (followed by Richardson extrapolation analysis) is necessary to provide a definitive benchmark for assessing the efficacy of the grid adaptation process in OVERFLOW. Yet, the comparison of the predictions based on the finest baseline, globally refined meshes employed in this paper with the force coefficients obtained via automatic adaptation was cost effective only when the starting baseline meshes were at level 2 or higher. This finding suggests the need for a minimum threshold resolution level for the baseline mesh used to begin the adaptation cycles. For the cases investigated here, the savings in grid count achieved with the adaptation process, are neither negligible nor adequate and also much smaller than those reported by Hildebrand et al.[13] for an anisotropic grid refinement. The isotropic adaptation process makes it difficult to discern if the streamwise or the wall-normal resolution is constraining the solution accuracy in a given region of the flow. Additional assessments not reported here suggest that the wall-normal resolution may be the more significant aspect for capturing the transition onset location as well as to enable grid convergence of the force coefficients when using the SST-based LM model. Thus, the ability to perform anisotropic adaptation is expected to facilitate further reduction in the overall grid count, and hence, in the cost of model verification studies. However, it must be mentioned that in OVERFLOW the adaptation is done automatically from within the flow solver, by taking advantage of the structured overset grid framework. This results in a quicker adaptation process, saving valuable computational time. This approach differs from the anisotropic adaptation using an external library[13]. The preliminary results presented here should provide a useful basis for further development of the near-body adaptation mechanics within OVERFLOW and for its application to help obtain grid-insensitive results for viscous flows with laminar-to-turbulent boundary-layer transition.

## **Acknowledgments**

This research is sponsored by the NASA Transformational Tools and Technologies (TTT) project of the Transformative Aeronautics Concepts Program under the Aeronautics Research Mission Directorate. The first author was supported by the NASA LaRC Research, Science, and Engineering Services (RSES) contract with Analytical Mechanics Associates. The authors would like to thank Pieter

**Twelfth International Conference on  
Computational Fluid Dynamics (ICCFD12),  
Kobe, Japan, July 14-19, 2024**

Buning of NASA Langley for valuable assistance through this effort. The computing resources used in this research was provided by the NASA Langley Research Center's K-Midrange Cluster.

## **References**

**Twelfth International Conference on  
Computational Fluid Dynamics (ICCFD12),  
Kobe, Japan, July 14-19, 2024**

- [1] Slotnick, J., Khodahoust, A., Alonso, J., Darmofal, D., Gropp, W., and Mavriplis, D., “CFD Vision 2030 Study: A Path to Revolutionary Computational Aerosciences,” NASA/CR-2014-218178, 2014.
- [2] Langtry, R. B. and Menter, F. R., “Correlation-Based Transition Modeling for Unstructured Parallelized Computational Fluid Dynamics Codes,” *AIAA Journal*, Vol. 47, No. 12, 2009, pp.2894–2906. <https://doi.org/10.2514/1.42362>
- [3] Coder, J.G. and Maughmer, M.D., “Computational Fluid Dynamics Compatible Transition Modeling Using an Amplification Factor Transport Equation,” *AIAA Journal*, Vol. 52, No. 11, 2014, pp.2506–2512. <https://doi.org/10.2514/1.J052905>
- [4] Menter, F. R., Smirnov, P. E., Liu, T., and Avancha, R., “A One-Equation Local Correlation-Based Transition Model,” *Flow, Turbulence and Combustion*, Vol. 95, No. 4, 2015, pp.583–619. <https://doi.org/10.1007/s10494-015-9622-4>
- [5] Venkatachari, B. S., Denison, M., Mysore, P. V., Hildebrand, N., and Choudhari, M. M., “Verification of the  $\gamma$ -Re $\theta$ t Transition Model in OVERFLOW and FUN3D,” *AIAA Journal of Aircraft*, Vol. 61, No.2, March-April 2024. <https://doi.org/10.2514/1.C037445> .
- [6] McRae, D. S., “r-Refinement Grid Adaptation Algorithms and Issues,” *Computer Methods in Applied Mechanics and Engineering*, Vol. 189, 2000, pp. 1161-1182. [https://doi.org/10.1016/S0045-7825\(99\)00372-2](https://doi.org/10.1016/S0045-7825(99)00372-2)
- [7] Löhner, T., “An Adaptive Finite Element Scheme for Transient Problems in CFD,” *Computer Methods in Applied Mechanics and Engineering*, Vol. 61, 1987, pp. 323-338. [https://doi.org/10.1016/0045-7825\(87\)90098-3](https://doi.org/10.1016/0045-7825(87)90098-3)
- [8] Baker, T. J., “Mesh Adaptation Strategies for Problems in Fluid Dynamics,” *Finite Elements in Analysis and Design*, Vol. 25, No. 3, 1997, pp. 243–273. [https://doi.org/10.1016/S0168-874X\(96\)00032-7](https://doi.org/10.1016/S0168-874X(96)00032-7)
- [9] Roy, C., “Strategies for Driving Mesh Adaptation in CFD (Invited), AIAA Paper 2009-1302, 2009. <https://doi.org/10.2514/6.2009-1302>
- [10] Fidkowski, K. J., and Darmofal, D. L., “Review of Output-Based Error Estimation and Mesh Adaptation in Computational Fluid Dynamics,” *AIAA Journal*, Vol. 49, No. 4, 2011, pp. 673–694. <https://doi.org/10.2514/1.J050073>
- [11] Park, M. A., Alauzet, F., and Michal, T., “HLPW-4/GMGW-3: Mesh Adaptation for RANS Technology Focus Group Workshop Summary,” *Journal of Aircraft*, Vol. 60, No. 4, 2023, pp. 1219–1237. <https://doi.org/10.2514/1.C037192>
- [12] Park, M. A., Loseille, A., Krakos, J., Michal, T. R., and Alonso, J. J., “Unstructured Grid Adaptation: Status, Potential Impacts, and Recommended Investments Towards CFD 2030,” AIAA Paper 2016-3323. <https://doi.org/10.2514/6.2016-3323>
- [13] Hildebrand, N., Mysore, P. V., Choudhari, M. M., and Paredes, P., “Grid Refinement Techniques for the  $\gamma$ -Re $\theta$ t Transition Model in FUN3D,” AIAA Paper 2024-2517, 2024. <https://doi.org/10.2514/6.2024-2517>
- [14] Gosin, S. A., Coder, J. G., Galbraith, M. C., Allmaras, S. R., and Wyman, N. J., “Assessment of Amplification Factor Transport Transition Modeling using Output-Based Mesh Adaptation,” AIAA Paper 2024-1157, 2024. <https://doi.org/10.2514/6.2024-1157>
- [15] Nichols, R. H. and Buning, P. G., “User’s Manual for OVERFLOW 2.3, Version 2.3,” NASA Langley Research Center, Hampton, VA, Oct 2019.
- [16] Buning, P. G. and Pulliam, T.H., “Near-Body Grid Adaptation for Overset Grids,” AIAA Paper 2016-3326, 2016. <https://doi.org/10.2514/6.2016-3326>
- [17] Meakin, R. L., “An Efficient Means of Adaptive Refinement Within Systems of Overset Grids,” AIAA Paper 95-1722, 1995. <https://doi.org/10.2514/6.1995-1722>
- [18] Menter, F. R., Kuntz, M., and Langtry, R., “Ten Years of Industrial Experience with the SST Turbulence Model,” *Turbulence, Heat and Mass Transfer*, Vol. 4 (1), 2003, pp. 625-632. [http://cfm.mace.manchester.ac.uk/flomania/pds\\_papers/file\\_pds-1068134610Menter-SST-paper.pdf](http://cfm.mace.manchester.ac.uk/flomania/pds_papers/file_pds-1068134610Menter-SST-paper.pdf)
- [19] Langtry, R. B., Sengupta, K., Yeh, D. T., and Dorgan, A. J., “Extending the Correlation based  $\gamma$ -Re $\theta$ t Transition Model for Crossflow Effects,” AIAA Paper 2015-2474, 2015. <https://doi.org/10.2514/6.2015-2474>
- [20] Coder, J.G., “Further Development of the Amplification Factor Transport Transition Model for Aerodynamic Flows,” AIAA Paper 2019-0039, 2019. <https://doi.org/10.2514/6.2019-0039>
- [21] Spalart, P. R. and Allmaras, S. R., “A One-Equation Turbulence Model for Aerodynamic Flows,” *Recherche Aerospaciale*, No. 1, 1994, pp. 5-21. <https://doi.org/10.2514/6.1992-439>
- [22] Medida, S., and Baeder, J., “Application of the Correlation-based the  $\gamma$ -Re $\theta$ t Transition Model to the Spalart-Allmaras Turbulence Model,” AIAA Paper 2011-3979, 2011. <https://doi.org/10.2514/6.2011-3979>
- [23] Childs, M. L., Pulliam, T. H., and Jespersen, D. C., “OVERFLOW Turbulence Model Resource Verification Results,” NASA Technical Report: NAS-2014-03, 2014.

**Twelfth International Conference on  
Computational Fluid Dynamics (ICCFD12),  
Kobe, Japan, July 14-19, 2024**

- [24] Roe, P. L., "Approximate Riemann Solvers, Parameter Vectors, and Difference Schemes," *J. Comput. Phys.*, Vol. 43, No. 2, 1981, pp. 357–372. [https://doi.org/10.1016/0021-9991\(81\)90128-5](https://doi.org/10.1016/0021-9991(81)90128-5)
- [25] Nichols, R. H., Tramel, R. W., and Buning, P. G., "Solver and Turbulence Model Upgrades to OVERFLOW 2 for Unsteady and High-Speed Applications," AIAA Paper 2006-2824, 2006. <https://doi.org/10.2514/6.2006-2824>
- [26] Derlaga, J. M., Jackson, C. W., and Buning, P. G., "Recent Progress in OVERFLOW Convergence Improvements," AIAA Paper 2020-1045, 2022. <https://doi.org/10.2514/6.2020-1045>
- [27] Dannenhoffer, I. and Baron, J., "Grid Adaptation for the 2-D Euler Equations," AIAA Paper 1985-484, 1985. <https://doi.org/10.2514/6.1985-484>
- [28] Spalart, P. R. and Rumsey, C. L., "Effective Inflow Conditions for Turbulence Models in Aerodynamic Calculations," *AIAA Journal*, Vol. 45, 2022, pp. 683-715. <https://doi.org/10.2514/1.29373>
- [29] Nie, S., "Extension of Transition Modeling by a Transport Equation Approach," Dissertation, DLR-Forschungsbericht, DLR-FB 2017-31, May 2017. [http://elib.dlr.de/113724/1/Ph.D\\_thesis\\_ShengyangNie\\_final%20print%20version\\_20170616.pdf](http://elib.dlr.de/113724/1/Ph.D_thesis_ShengyangNie_final%20print%20version_20170616.pdf)
- [30] Schubauer, G. B., and Skramstad, H. K., "Laminar Boundary Layer Oscillations and Stability of Laminar Flow," *J. Aero. Sci.*, Vol. 14, No. 2, 1947, pp. 69–78. <https://doi.org/10.2514/8.1267>
- [31] Somers D. M., "Design and Experimental Results for the S809 Airfoil," NREL SR-440-6918, 1997.
- [32] Coder, J. G., "Standard Test Cases for CFD-Based Laminar-Transition Model Verification and Validation," AIAA Paper 2018-0029, 2018. <https://doi.org/10.2514/6.2018-0029>
- [33] "NLR 7301 Airfoil," Experimental Data Base for Computer Program Assessment, AGARD Rept. AR-138, Neuilly sur Seine, France, 1979.